High Transmission in 120-degree Sharp Bends of Inversion-symmetric and Inversion-asymmetric Photonic Crystal Waveguides

Wei Dai[1,2], Taiki Yoda[1,2], Yuto Moritake[1], Masaaki Ono[2,3], Eiichi Kuramochi[2,3], and Masaya Notomi[1,2,3,*]

[1]Department of Physics, Tokyo Institute of Technology, 2-12-1 Ookayama, Meguro-ku, Tokyo 152-8550, Japan
[2]NTT Basic Research Laboratories, NTT Corporation, 3-1 Moriosato-Wakamiya, Atsugi, 243-0198, Japan
[3]Nanophotonics Center, NTT Corporation, 3-1 Moriosato-Wakamiya, Atsugi, 243-0198, Japan
[*]E-mail: notomi@phys.titech.ac.jp

1. Simulation method

As shown in Fig.1(a) the PhCWGs are surrounded by perfectly matched layers (PMLs). The total length of each waveguide is 100a. A unidirectional dipole source is put inside each waveguide, perpendicular to the waveguide direction, to excite the waveguide modes. The width of the dipole source is set to 2a. We have confirmed that changing wave source width does not affect the simulation results. The source is a combination of surface electric current and surface magnetic current. Surface current density $Js = (0, \sqrt{2n_{eff}}/\sqrt{Z_0 L_{dipole}}, 0)$ Surface magnetic current density: $Jms = (0, 0, \sqrt{2Z_0}/\sqrt{n_{eff} L_{dipole}})$ where n_{eff} is the effective refractive index, L is the dipole length and Z_0 is the impedance in free space. By fixing the ratio $Jms/Js = Z_0/n_{eff}$, we excite an EM wave propagating only rightwards.

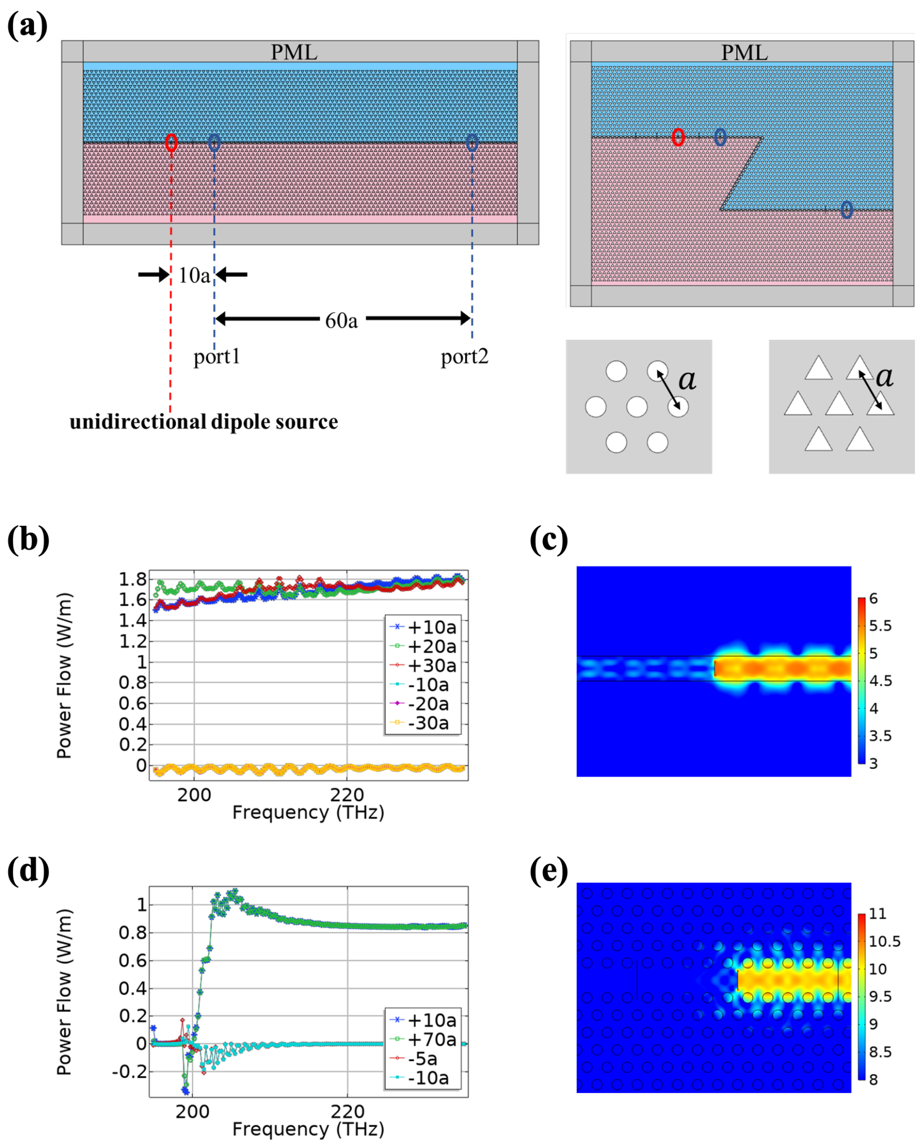

Figure 1. (a) Schematic illustration of straight band bend waveguides in numerical calculation. The unidirectional dipole sources are positioned inside the red circles. 2 observation ports, port-1, and port-2 are positioned inside blue circles. The PhCWGs are surrounded by PMLs. Left is the straight waveguide and right is the Z-shaped bent waveguide with two 120-degree sharp bends. The bottom right is the enlarged bulk triangular lattice with and without inversion. (b) Power flow spectra of a silicon waveguide. The excited wave is assumed to propagate right-wards. 3 ports are set at each of the left and right sides of the dipole wave source, each 10a, 20a, and 30a away from the source. (c) The E-field intensity of the excited wave in the silicon waveguide at 200THz. (d) Power flow spectra of the W1WG are discussed in the simulation results. (e) The E-field intensity of the excited wave in the W1WG at 210THz

In the straight waveguide, 2 observation ports, port-1, and port-2 are located 10a and 70a away from the wave source. In the bent waveguide, port-1 is located 10a away and the first sharp bend is 30a away from the wave source. The second sharp bend is 20a away from the first one. And port-2 is 20a away from the second sharp bend. Thus, the observed EM waves travel the same distance between port-1 and port-2 in straight and bent waveguides. The source power P_0 is calculated as the total power flow (Poynting vector) orthogonal to port-1 in the straight waveguide. The transmitted power in a straight waveguide P_s and that in the Z-shaped waveguide P_z are calculated as the total power flow orthogonal to port-2 at each waveguide. The transmittance is calculated as P_s/P_0 in straight waveguides and P_z/P_0 in Z-shaped waveguides. We cannot calculate the bend-transmittance naively as P_z/P_1 where P_1 is the total power flow passing through port-1 in the Z-shaped waveguide. The reason is that P_1 also collects the power of reflected waves at the bends and is strongly affected by the F-P resonance. To examine the unidirectionality of the dipole source, we first confirm the wave propagation in a rectangular silicon waveguide without photonic crystal. The waveguide width is $\sqrt{3}a$. As shown in Fig.1(b), the energy flow observed at the left-side ports (-10a, -20a, and -30a) is less than 10% of that observed at the right-side ports (10a,20a,30a). The E-field intensity at 200THz is plotted in Fig.1(c) in logarithm scale. We can see the majority of the energy propagates right-wards. In Fig.1(d,e), we have confirmed the same unidirectionality of a straight W1WG.

2. Other simulation results

We have reported in Table.1 and Fig.6(a) in the main manuscript the simulation results of $S=-1$, $S=1$, $S=2$ IS- and IA-PhCWGs, and $S=3$ IA-PhCWGs. $S=-1$ and $S=1$ PhCWGs have high transmissions, and $S=2$ and $S=3$ PhCWGs have lob transmissions via 120-degree sharp bends. Here we discuss these results in detail.

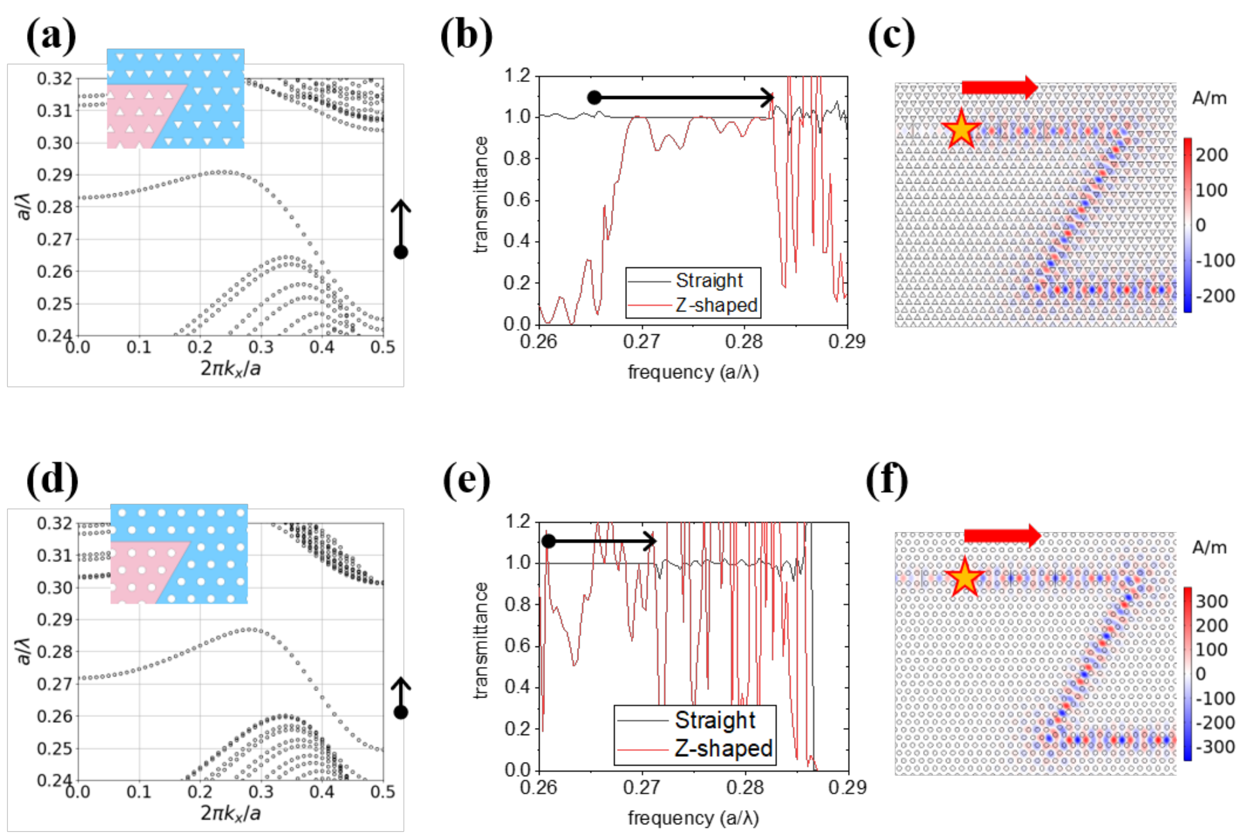

Figure 2. Calculation results of the straight and Z-shaped $S=1$ PhCWGs. (a) PBS of the $S=1$ IA-PhCWG. (b) The transmittance spectra of the straight $S=1$ IA-PhCWG (black curve) and Z-shaped bent $S=1$ IA-PhCWG (red curve). The T_{av} is 0.94. The R_{FP} is 0.04. (c) The out-of-plane magnetic field H_z of a Z-shaped $S=1$ IA-PhCWG at $a/\lambda=0.272$ with a transmittance of 0.88. (d) PBS of the $S=1$ IS-PhCWG. The black arrow shows the single-mode region. The inset shows one corner of the bent waveguide. (e) The transmittance spectra of the straight $S=1$ IS-PhCWG (black curve) and Z-shaped bent $S=1$ IS-PhCWG (red curve). The T_{av} is 1. The R_{FP} is 0.14. (f) The out-of-plane magnetic field H_z of a Z-shaped $S=1$ IS-PhCWG at $a/\lambda=0.267$ with transmittance of 0.90.

(i) $S = 1$, mirror-symmetric waveguides

$S = 1$ waveguides have zigzag interfaces. This domain-wall configuration appears in many previous VPhC studies, reporting the high transmission in Z-shaped $S = 1$ PhCWGs with honeycomb lattice[1–4]. As shown in Fig.2 (a,d), the single-mode region is 0.260-0.272 in the IS-PhCWG and 0.266-0.283 in the IA-PhCWG. As shown in Fig.2(b,e), the transmittances of Z-shaped $S = 1$ IS-PhCWG and $S = 1$ IA-PhCWG are both very high compared to that of the W1WG. The $S = 1$ IS-PhCWG has T_{av} of 1.00 and R_{FP} of 0.14. The $S = 1$ IA-PhCWG has T_{av} of 0.94 and R_{FP} of 0.04. Note that the bend-transmittance of $S = 1$ IS-PhCWG is greater than 1 at some frequencies and averages 1.00 despite strong fluctuation in the spectrum. This is due to bad coupling between the waveguide mode and the wave source and the subsequent complicated F-P resonance. We can see from Fig.2(c) that the waveguide mode is well confined in the $S = 1$ IS-PhCWG, and the majority of wave flux travels through the Z-shaped bends without much scattering. Despite the technical issues in the numerical calculation, we can conclude that the $S = 1$ IS-PhCWG has good bend-transmission comparable to that of the $S = 1$ IA-PhCWG and $S = 3$ PhCWGs.

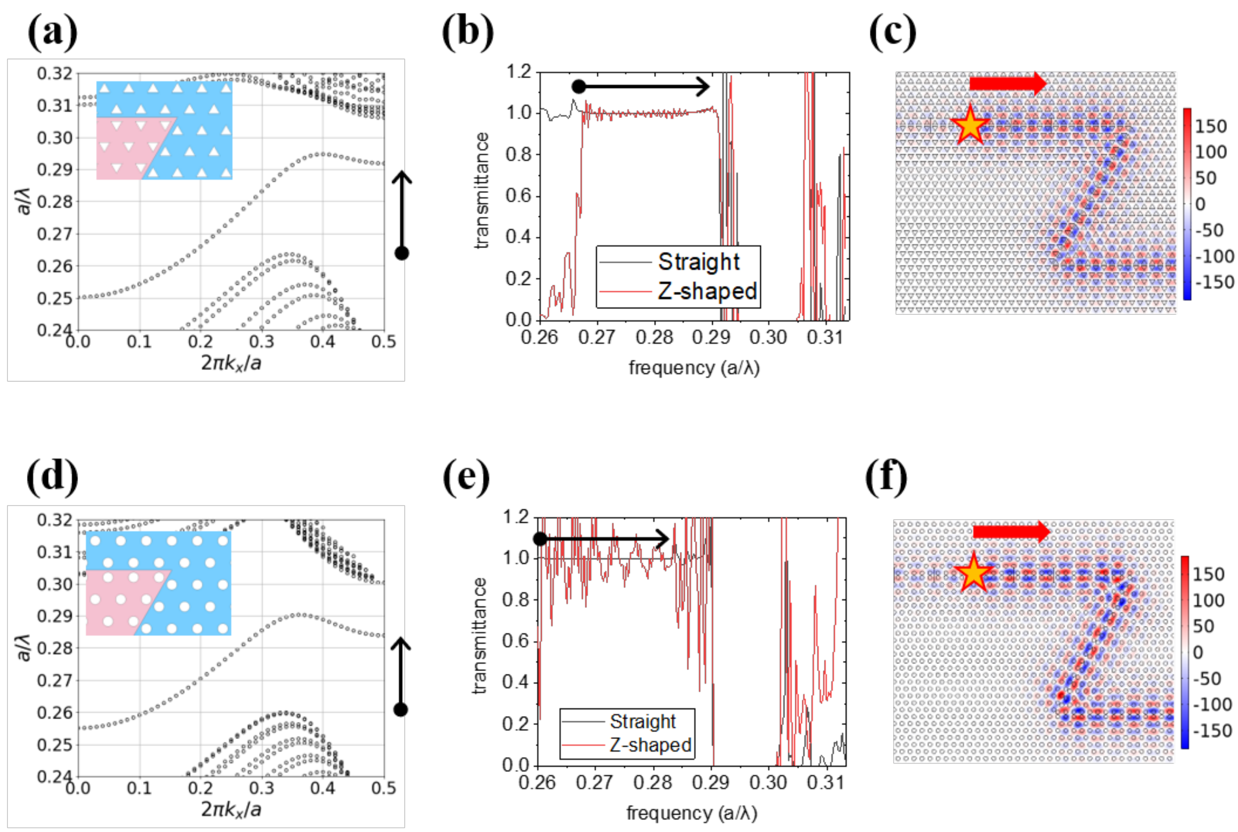

Figure 3. Calculation results of the straight and Z-shaped $S = -1$ PhCWGs. (a) PBS of the $S = -1$ IA-PhCWG. (b) The transmittance spectra of the straight $S = -1$ IA-PhCWG (black curve) and Z-shaped bent $S = -1$ IA-PhCWG (red curve). The T_{av} is 1.00. The R_{FP} is 0.03. (c) The out-of-plane magnetic field of a Z-shaped $S = -1$ IA-PhCWG at $a/\lambda = 0.277$ with a transmittance of 0.97. (d) PBS of the $S = -1$ IS-PhCWG. The black arrow shows the single-mode region. The inset shows one corner of the bent waveguide. (e) The transmittance spectra of the straight $S = -1$ IS-PhCWG (black curve) and Z-shaped bent $S = -1$ IS-PhCWG (red curve). The T_{av} is 1.00. The R_{FP} is 0.17.(f) The out-of-plane magnetic field of a Z-shaped $S = -1$ IS-PhCWG at $a/\lambda = 0.273$, with a transmittance of 0.96.

(ii)S = -1, mirror-symmetric waveguides

$S = -1$ PhCWGs have another type of zigzag interface where the lattice configuration is more compact. Similar to that in the honeycomb lattice ones[5–7], the waveguide mode has odd spatial parity about the central waveguide line. As shown in Fig.3(a), the $S = -1$ IA-PhCWG has a wide single mode in $a/\lambda = 0.263 - 0.292$. As shown in Fig.3(b), the transmittance is very high throughout the whole single-mode region with weak F-P ripples. The T_{av} is 1.00. The R_{FP} is 0.03. Figure3(c) shows

H_z distribution at $a/\lambda = 0.267$, where the transmittance is 0.90. The simulated results of $S = -1$ IA-PhCWG agree well with a recent report by He et al.[8].

S = -1 IS-PhCWG has a single-mode region in $a/\lambda = 0.260 - 0.284$. As shown in Fig.3(e), the bend-transmittance fluctuates around unity with obvious F-P ripples in the spectrum. The cause of this irregular spectrum is the same as that for the $S = 1$ IS-PhCWG. The T_{av} of $S = -1$ IS-PhCWG is 1.00, and the R_{FP} is 0.17. Figure5(f) shows H_z distribution at $a/\lambda = 0.273$, where the transmittance is 0.96. Similar to the $S = 1$ and $S = -2$ waveguides, the $S = -1$ PhCWGs have high bend-transmission regardless of the inversion symmetry in the bulk lattice.

(iii)S = 2, glide-symmetric waveguides

S=2 PhCWGs correspond to another type of bearded interface[9–13] other than S=-2 waveguides. It has been reported that the lower band of this domain-wall type in honeycomb-lattice VPhCs has high bend-transmission while the upper band has low bend-transmission[9,11,13]. Here, in a triangular lattice PhCWG, the lower band has no single-mode region. Here, we focus only on the upper band. As shown in Fig.4(a,d), the single-mode region is 0.271-0.301 for IS-PhCWG and 0.277-0.306 for IA-PhCWG. As shown in Fig.4(b,e), both $S = 2$ PhCWGs have low bend-transmission in the upper band. The T_{av} is 0.33 for IA-PhCWG and 0.14 for IS-PhCWG, both lower than that of a W1WG. The calculated R_{FP} is 1.00 for both IA-PhCWG and IS-PhCWG. Figure4(c) shows the H_z distribution of $S = 2$ IA-PhCWG at $a/\lambda = 0.285$, where the transmittance is 0.39. Figure4(f) shows the H_z distribution of $S = 2$ IS-PhCWG at $a/\lambda = 0.279$, where the transmittance is 0.17. In Fig.4(c,f), there is an apparent intensity attenuation during propagation and strong backscattering at the left side of the wave sources.

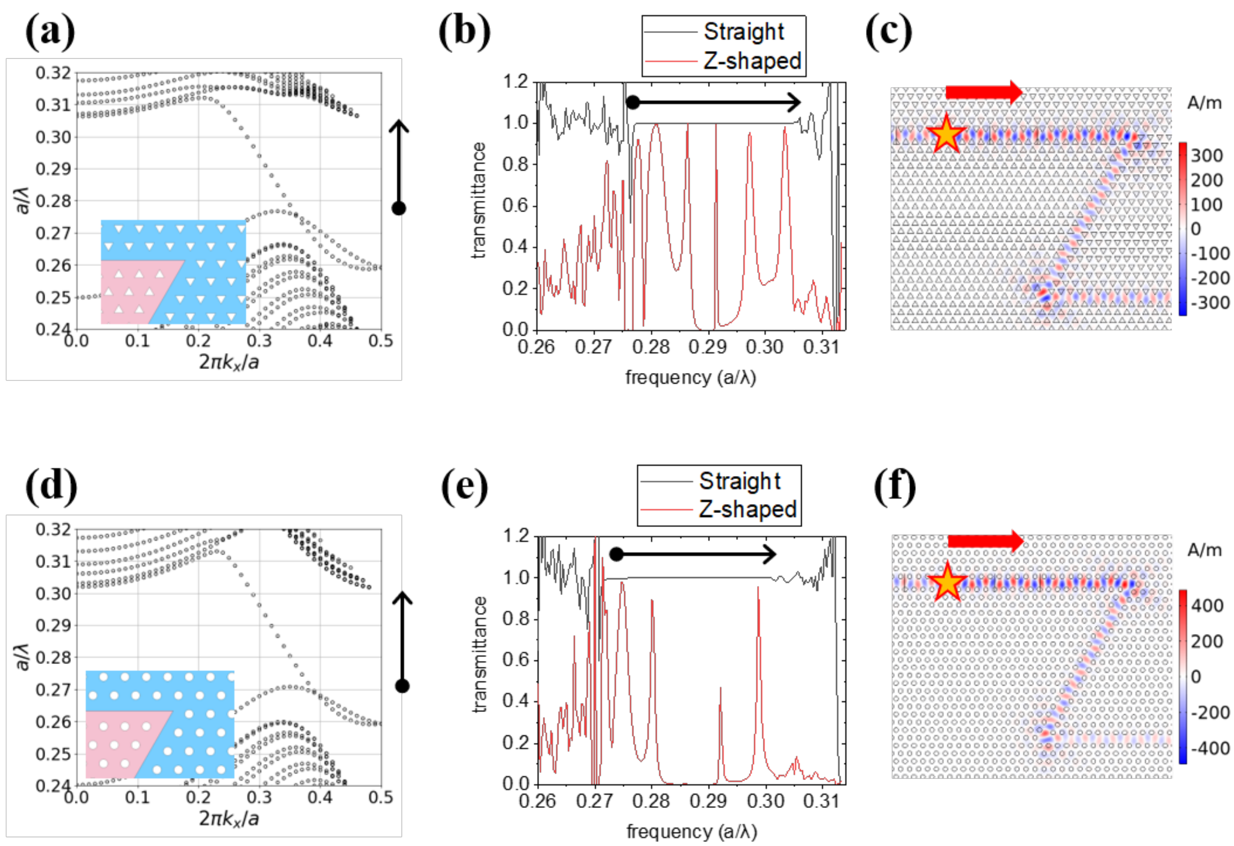

Figure 4. Calculation results of the straight and Z-shaped $S = 2$ PhCWGs. (a) PBS of the $S = 2$ IS-PhCWG. The black arrow shows the single-mode region. The inset shows one corner of the bent waveguide. (b) The transmittance spectra of the straight $S = 2$ IS-PhCWG (black curve) and Z-shaped bent $S = 2$ IS-PhCWG (red curve). (c) The out-of-plane magnetic field of a Z-shaped $S = 2$ IS-PhCWG at $a/\lambda = 0.279$ with a transmittance of 0.17. (d) PBS of the $S = 2$ IA-PhCWG. (e) The transmittance spectra of the straight $S = 2$ IA-PhCWG (black curve) and Z-shaped bent $S = 2$ IA-PhCWG (red curve). (f) The out-of-plane magnetic field of a Z-shaped $S = 2$ IA-PhCWG at $a/\lambda = 0.285$ with a transmittance of 0.39.

In this waveguide design, we are not able to evaluate the lower band of $S=2$ PhCWGs. However, one can obtain single modes for both bands in an $S=2$ PhCWG by locally changing the diameter of air holes along the waveguide interface. For a full comparison with the previous VPhCWGs, we discuss the hole-resized $S=2$ PhCWGs in section 3.

(iv)S = 3, mirror-symmetric waveguides without inversion symmetry

Finally, we return to $S=3$ PhCWG with triangular holes (broken inversion symmetry). Similar to $S=3$ IS-PhCWG (W1WG), the lower band has a wide single-mode region. This interface does not correspond to any conventional VPhCWGs. As shown in Fig.5(a), the single-mode region is 0.270-0.293. As shown in Fig.5(b), the bend-transmission is very low. The T_{av} is 0.41. The R_{FP} is 0.56. Figure5(c) shows the H_z distribution of $S=3$ IA-PhCWG at $a/\lambda=0.275$, where the transmittance is 0.58. There is an apparent attenuation and distortion of the H_z in the propagation and strong backscattering at the left side of the wave source.

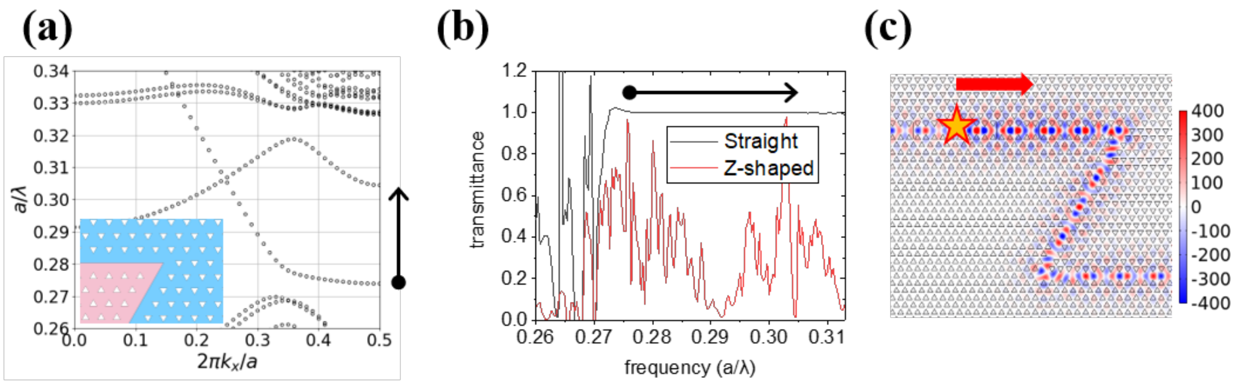

Figure 5. Calculation results of the straight and Z-shaped $S=3$ IA-PhCWGs. (a) PBS of the $S=3$ IA-PhCWG. The black arrow shows the single-mode region. The inset shows one corner of the bent waveguide. (b) The transmittance spectra of the straight $S=3$ IA-PhCWG (black curve) and Z-shaped bent $S=3$ IA-PhCWG (red curve). The T_{av} is 0.41. The R_{FP} is 0.56. (c) The out-of-plane magnetic field of a Z-shaped $S=3$ IA-PhCWG at $a/\lambda=0.275$ with a transmittance of 0.58.

2. Excluding trivial factors

We have discussed the influence of domain-wall types and inversion symmetry breaking on bend-transmission. In Table 1 we demonstrate that other factors such as spatial parity, the waveguide width, group refractive index (n_g), and band index do not affect the bend-transmission of waveguide modes. While it is known that bend scattering is strong in slow light regions, the focus of this work is the overall performance of waveguide bands in a broad wavelength range. The n_g here is calculated at the middle of the single-mode region for each waveguide band. We can see that the waveguide mode can have either high bend-transmittance or low bend-transmittance regardless of the value of n_g. The same can be observed for other properties like spatial parity and band index.

<table>
<tr><td rowspan="2">Interface type</td><td colspan="2">shifting parameter</td><td colspan="2">S=-2</td><td>S=-1</td><td>S=1</td><td colspan="2">S=2</td><td>S=3</td></tr>
<tr><td colspan="2">waveguide width($\sqrt{3}$a)</td><td colspan="2">1/6</td><td>1/3</td><td>2/3</td><td colspan="2">5/6</td><td>1</td></tr>
<tr><td rowspan="8">Properties of guided-modes</td><td colspan="2">parity of Hz</td><td colspan="2">mixed</td><td>odd</td><td>even</td><td colspan="2">mixed</td><td>even</td></tr>
<tr><td colspan="2">band index</td><td>lower</td><td>upper</td><td></td><td></td><td>lower</td><td>upper</td><td></td></tr>
<tr><td rowspan="3">with I-symmetry ○</td><td>n_g</td><td>5.2-15</td><td>3.9-5.2</td><td>6.3-11.3</td><td>3.6-4.1</td><td>6.8-254</td><td>3.5-5.4</td><td>2.5-250</td></tr>
<tr><td>Sign of v_g</td><td>+</td><td>−</td><td>+</td><td>−</td><td>+</td><td>−</td><td>−</td></tr>
<tr><td>Bend transmittance</td><td>✗</td><td>✓</td><td>✓</td><td>✓</td><td>✓</td><td>✗</td><td>✗</td></tr>
<tr><td rowspan="3">without I-symmetry △</td><td>n_g</td><td></td><td>3.8-5.2</td><td>5.4-7.2</td><td>3.3-4.7</td><td>6.2-7.3</td><td>3.3-5.2</td><td>3.2-572</td></tr>
<tr><td>Sign of v_g</td><td></td><td>−</td><td>+</td><td>−</td><td>+</td><td>−</td><td>−</td></tr>
<tr><td>Bend transmittance</td><td></td><td>✓</td><td>✓</td><td>✓</td><td>✓</td><td>✗</td><td>✗</td></tr>
</table>

Table 1. Summary of properties of waveguide modes by their domain-wall types (S parameters) and bulk lattice symmetry. Check marks indicate high and "X" marks indicate low bend transmittance.

3. Resizing air holes

By locally resizing the air holes in the PhCWG, we can further engineer the band structure. Here we demonstrate 2 examples: the shrunken S=0 PhCWG and the expanded $S = 2$ PhCWG.

i) The shrunken S=0 PhCWG

Without lattice shifting, we directly introduce a defect to the bulk triangular lattice by shrinking 2 arrays of air holes along the ΓK direction, as shown in the inset image Fig.6(a). In the simulation, the lattice constant is 500 nm. The larger air holes in the bulk lattice have a radius of 136 nm, and the smaller air holes at the interface have a radius of 81 nm. The effective refractive index is 2.74. The shrunken S=0 PhCWGs have glide-symmetry along the interface. As shown in Fig.6(a), the band structure is more complicated than previously discussed waveguides, with 4 bands and 2 degeneracies in the bandgap. Here only one band has single modes at $a/\lambda = 0.309 - 0.315$. The bend-transmittance of this band is very high as shown with red curves in Fig.6(b). The T_{av} is 0.933. The R_{FP} is 0.149. We can also confirm from the H_z profile in Fig.6(c) that the bend-transmission is high with no apparent backward flux at the left side of the wave source (five-point star).

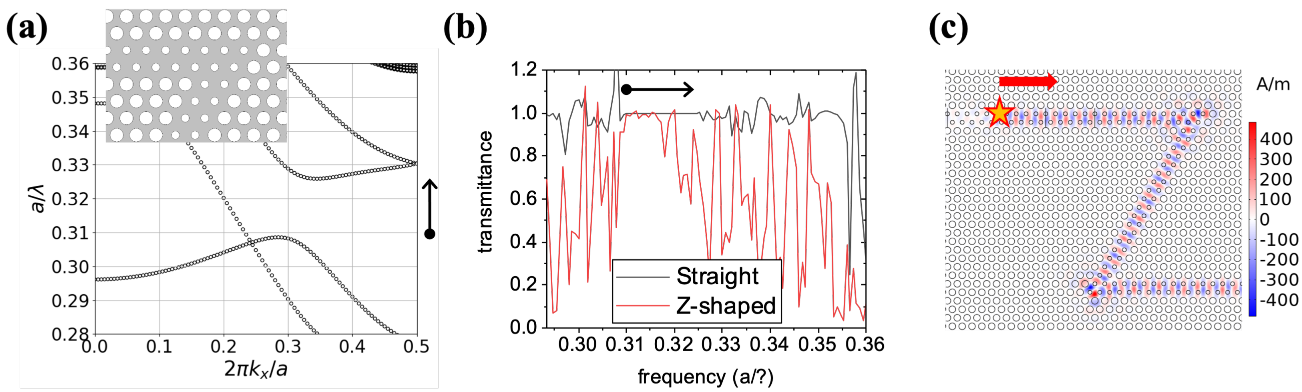

Figure 6. Calculation results of the straight and Z-shaped $S = 0$ IS-PhCWGs. (a) PBS of the $S = 0$ Cir-PhCWG. The black arrow shows the single-mode region. The inset shows one corner of the bent waveguide. The larger air holes in the bulk lattice have a radius of 136 nm. The small air holes have a radius of 81 nm. (b) The transmittance spectra of the straight $S = 0$ IS-PhCWG (black curve) and Z-shaped bent $S = 0$ IS-PhCWG (red curve). (c) The out-of-plane magnetic field of a Z-shaped $S = 0$ IS-PhCWG at $a/\lambda = 0.313$ with a transmittance of 1.00.

ii) The expanded $S = 2$ PhCWG

The expanded $S = 2$ PhCWGs have the same lattice configuration as the $S = 2$ PhCWGs except that the nearest 2 arrays of air holes along the interface have larger sizes than those in the bulk lattice. The $S = 2$ IS-PhCWGs have a lattice constant of 460 nm. The radius of larger holes is 204 nm. The radius of the smaller holes is 146 nm. The effective refractive index of silicon is set to be 2.7. As the hole size grows larger along the interface, the lower of the two touching bands rises up and forms a single-mode region, making it possible to investigate its transmission property (Fig.7(a)). As shown in Figure7(b) the lower band has high transmission through Z-shaped waveguides. The T_{av} is 1.00 in the upper band and 0.13 in the lower band. The R_{FP} is 0.18 in the lower band and 1.00 in the upper band.

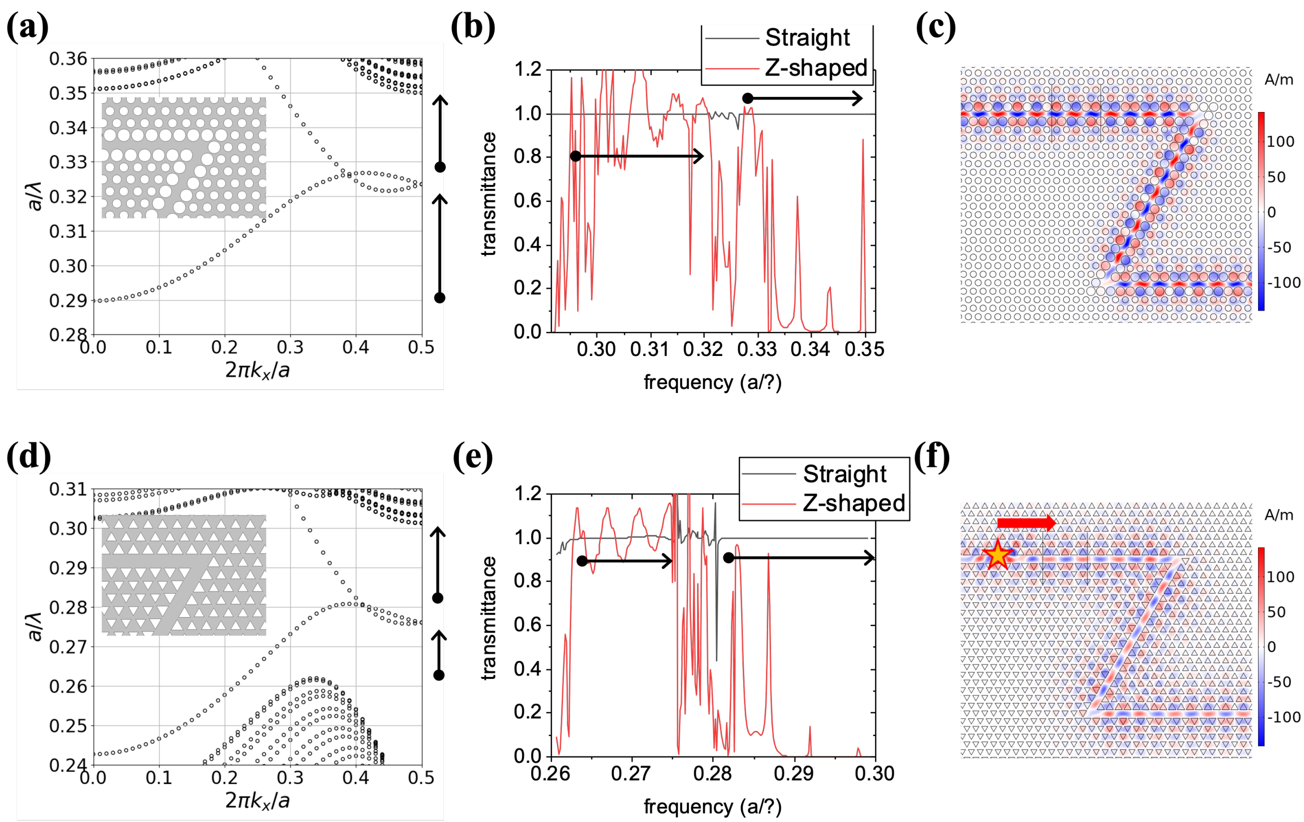

Figure 7. Calculation results of the straight and Z-shaped $S = 2$ PhCWGs. (a) PBS of the $S = 2$ IS-PhCWG. The black arrow shows the single-mode region. The inset shows one corner of the bent waveguide. The large air holes in the bulk lattice have a radius of 204 nm. The small holes have a radius of 146 nm. (b) The transmittance spectra of the straight $S = 2$ IS-PhCWG (black curve) and Z-shaped bent $S = 2$ IS-PhCWG (red curve). (c) The out-of-plane magnetic field of a Z-shaped $S = 2$ IS-PhCWG at $a/\lambda = 0.313$ with a transmittance of 0.96. (d) PBS of the $S = 2$ IA-PhCWG. The black arrow shows the single-mode region. The inset shows one corner of the bent waveguide. The large air holes in the bulk lattice have a side length of 381 nm. The small holes have a side length of 319 nm. (e) The transmittance spectra of the straight $S = 2$ IA-PhCWG (black curve) and Z-shaped bent $S = 2$ IA-PhCWG (red curve). (f) The out-of-plane magnetic field of a Z-shaped $S = 2$ IS-PhCWG at $a/\lambda = 0.267$ with transmittance of 1.

The $S = 2$ IA-PhCWGs have a lattice constant of 460 nm. The side length of the larger triangular holes is 382 nm. The side length of the smaller triangular holes is 319 nm. The effective refractive index of silicon is 2.7. Like the IS-PhCWGs, the lower band of IA-PhCWGs rises up due to the resizing of air holes, as shown in Fig.7(d). The T_{av} is 1.00 in the upper band and 0.05 in the lower band. The R_{FP} is 0.07 in the lower band and 1.00 in the upper band.

We have included the results of the hole-resized $S = 2$ PhCWGs in Table.1 and Fig.7 in the main manuscript.

4. Experiment setting

We conduct the transmission measurement of waveguides using the experimental setup shown in Fig.8. Light from a wavelength-tunable laser is collimated by lens 1 and obtains linear polarization through POL 1. The polarization direction can be adjusted by rotating the half-wave plate (HWP) 1. In our measurement, we set the orientation of the HWPs so that only TE waves are transmitted into the device. Then the incident light is focused by lens 2 and coupled to the waveguide. The transmitted light undergoes a reversed process and is collected by the power meter. The power meter measures light intensity in decibel-milliwatts. The measurable power is up to -110dBm. There are time-variant fluctuations in the measured intensity up to 1dBm. The measured spectra are smoothed using adjacent averaging to remove the irrelevant fluctuation in raw data.

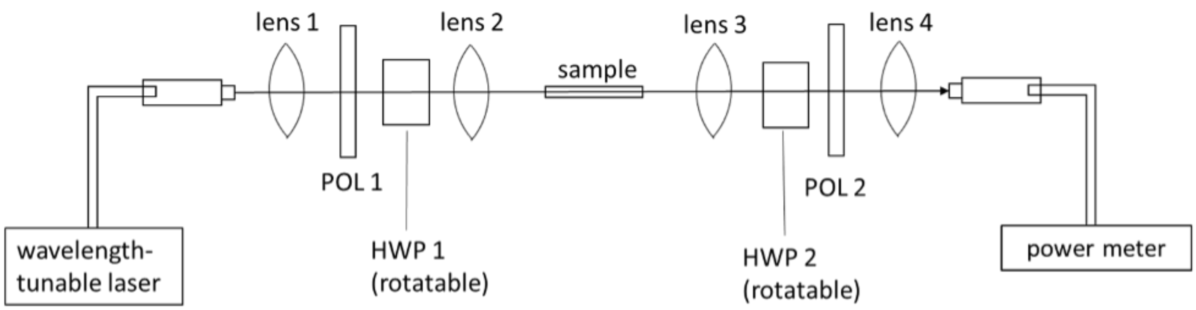

Figure 8. Schematic of the experimental setup. Light from a wavelength-tunable laser is collimated by lens 1 and obtains linear polarization through POL 1. The polarization direction can be adjusted by rotating the half-wave plate (HWP) 1.

5. Mode classification based on band structures

We have discussed various waveguides with integer S values. Actually, the S can be tuned continuously. We calculate the photonic band structure for various S values in a 3-dimensional Si PhC slab in Fig.9. As the shifting parameter S decreases continuously, the waveguide modes emerge from bulk modes below the PBG and move upwardly into the bulk modes above the PBG. Different bands can be traced to one another in this process. Thus, we can classify these bands into four groups as S changes from 3 to -2. The even mode of W1WG and the upper band of $S = 2$ glide-symmetric PhCWG belong to group 1 (green). The lower band of $S = 2$ glide-symmetric PhCWG and the even band of $S = 1$ PhCWG belong to group 2 (blue). The odd mode of $S = -1$ PhCWG and the upper band of $S = -2$ glide-symmetric PhCWG belong to group 3 (orange). Finally, the lower band of $S = -2$ glide-symmetric PhCWG belongs to group 4 (gray). Waveguide modes in group 1 and group 4 have low bend-transmission, and those in group 2 and group 3 have high bend-transmission. This mode classification originates from the photonic band structures (PBGs). Therefore, it is not self-evident that the bend-transmission via 120-degree bends is related to this mode classification.

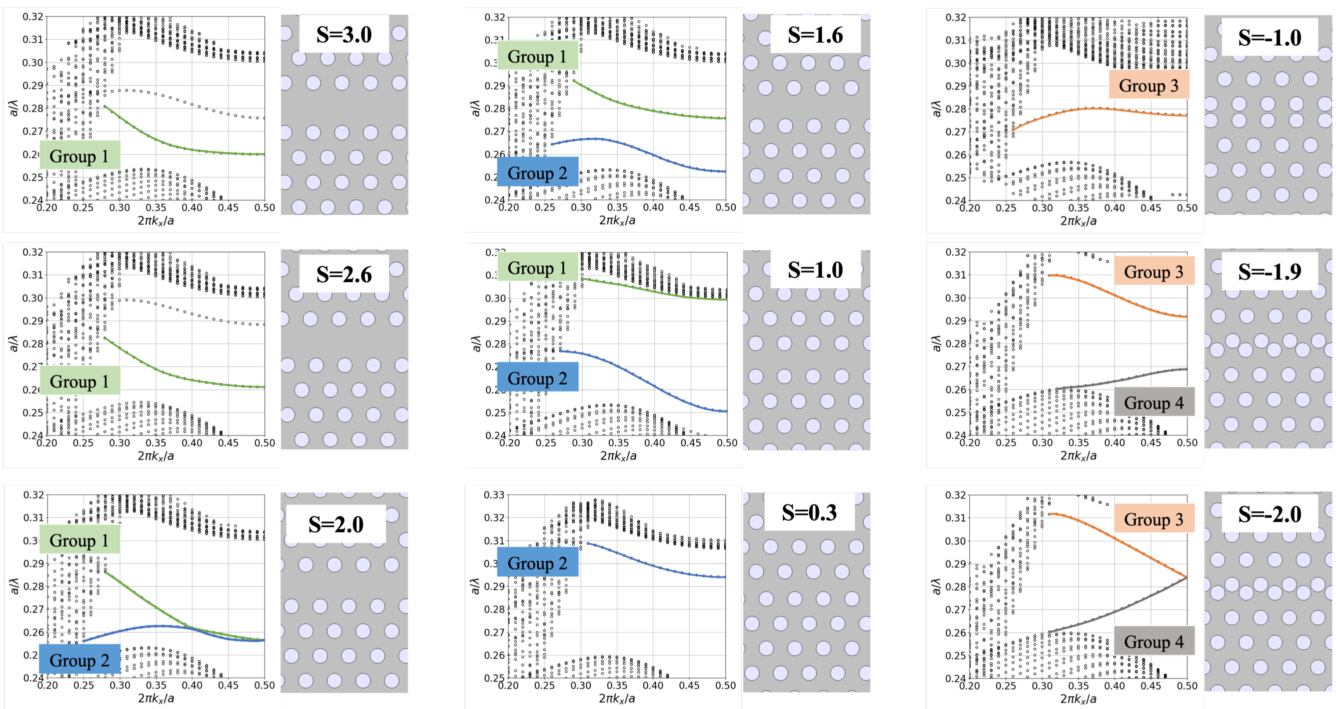

Figure 9. Band structure of PhCWGs of various domain-wall types as shifting parameter S changes continuously from 3 to -2. Bands of the same group can be traced to each other.

6. Simulation results of circular polarization singularities

We have investigated the spatial distribution of circular polarization singularities or C-points (CPs) for all domain-wall types discussed in the main text. Figure10 shows the CP distribution inside an $S = -2$ IA-PhCWG in the high bend-transmission band. The top four images show the zero-value isolines of the Stokes parameters, where the crossing node of the $S_1 = 0$ and $S_2 = 0$ lines represent the location of CPs. The bright CPs near the connection interface are marked with black boxes. The bottom images show the normalized E-field intensities at the corresponding frequencies. Below each image are the normalized frequencies (a/λ), normalized intensities at the location of the CPs, and the bend-transmittance of the Z-shaped waveguide. For waveguide modes at $a/\lambda = 0.269$ and $a/\lambda = 0.282$, there are bright CPs inside the first nearest air holes. At higher frequencies, the CPs disappear from these holes although the degree of polarization is still very high (over 0.99). New CPs appear inside the second nearest air holes. This change of locations differs from the case in $S = -2$ IS-PhCWGs, which indicates that the shape of air holes can modify the location of CPs to some extent.

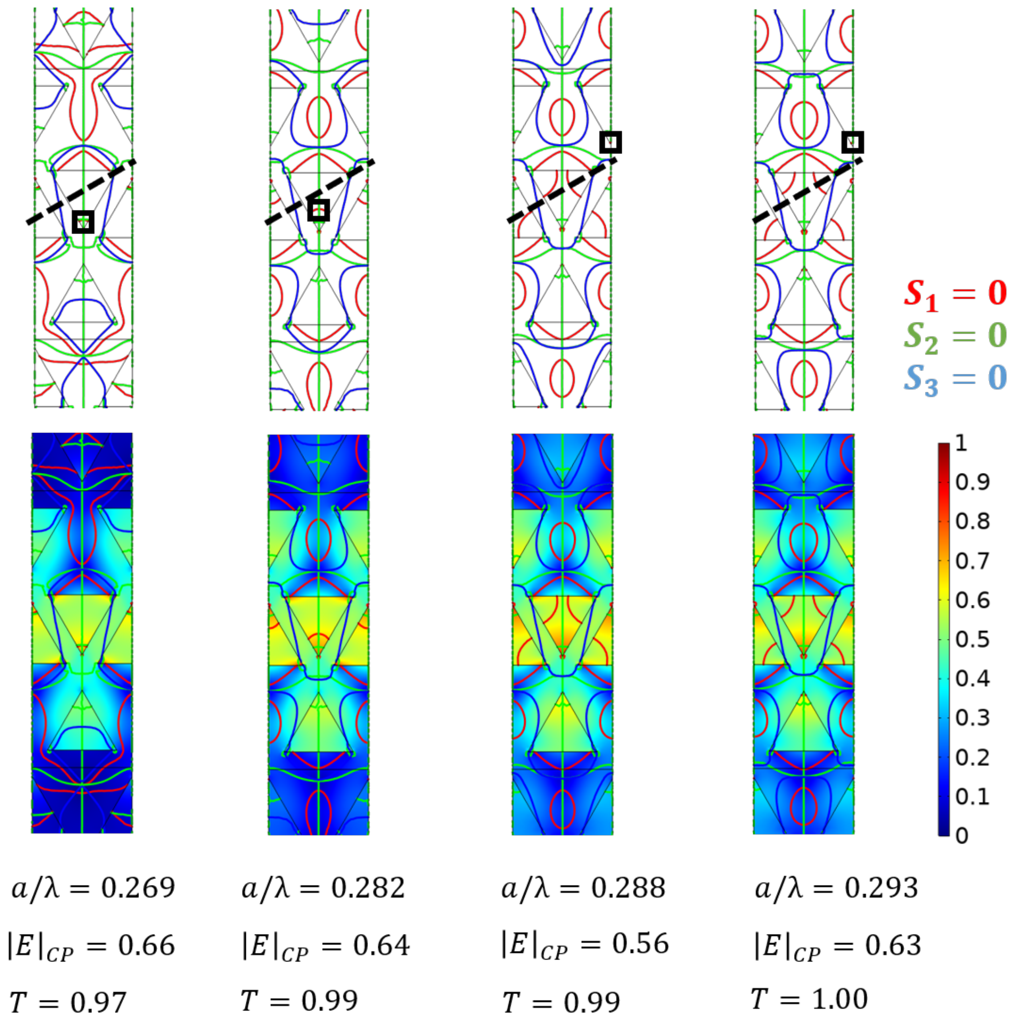

Figure 10. The zero-value isoline of Stokes parameters (top) and the Electric field amplitudes (bottom) of $S = -2$ IA-PhCWGs. The corresponding frequencies, normalized E-field amplitudes at the location of CPs, and the bend-transmittance are shown below each plot.

Figure11 shows the CP distributions inside $S = -1$ PhCWGs. The left six images show the $S = -1$ IS-PhCWGs and the right six images show the $S = -1$ IA-PhCWGs. In both cases, there are bright CPs inside the nearest air holes near the connection interfaces. Figure12 shows the case of $S = 1$ PhCWGs. The left two images show the result of $S = 1$ IS-PhCWGs. We plot the result of only one frequency for the $S = 1$ IS-PhCWG because the CPs and field intensities do not change much within the single-mode region due to the narrow waveguide band. The right six images show the result of $S = 1$ IA-PhCWGs. In the $S = 1$ PhCWGs, the bright CPs near the connection interface are located inside the silicon area instead of inside the

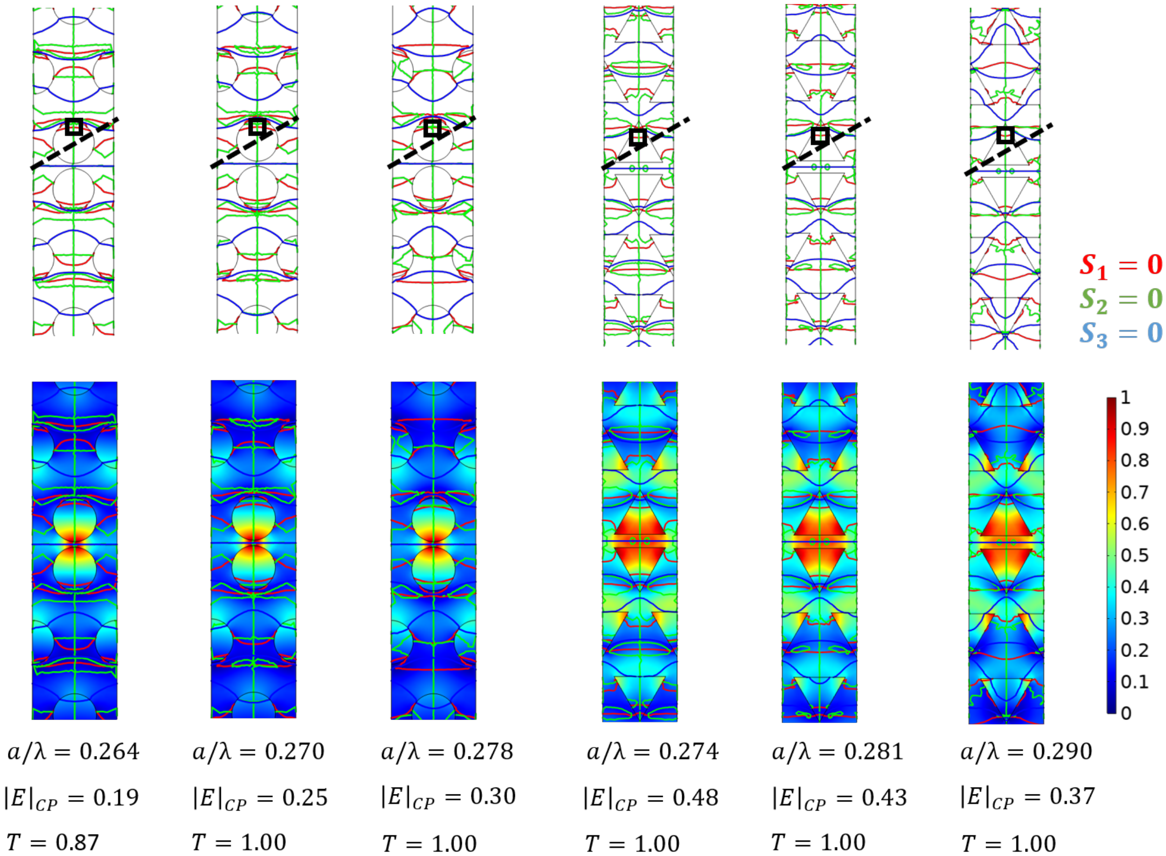

Figure 11. The zero-value isoline of Stokes parameters (top) and the Electric field amplitudes (bottom) of $S = -1$ IS- (left three columns) and IA-(right three columns) PhCWGs. The corresponding frequencies, normalized E-field amplitudes at the location of CPs, and the bend-transmittance are shown below each plot.

air holes. We speculate that CPs in the silicon areas are more susceptible to perturbations and less stable at the bends, which explains the relatively larger fluctuations in the transmittance spectra observed in the $S = 1$ PhCWGs. Actually, when we restore the second sublattice in the $S = 1$ PhCWGs (a zigzag interface PhCWG having a honeycomb lattice), there are also bright CPs at similar locations, except that these CPs fall within the air holes of the second sublattice. We have found that the simulated transmittance spectrum of the bent honeycomb lattice $S = 1$ PhCWG is more stable than its triangular lattice counterparts.

Figure13 shows the results of the $S = 2$ IS-PhCWGs. If we ignore the "unstable" CPs inside the silicon areas, we can see that the high bend-transmission band has bright CPs near the connection interface, which lies inside the air holes, while in the low bend-transmission band these bright CPs disappear. We apply the same rule to the S-3 PhCWGs and ignore the silicon region CPs. The left six images in Fig.14 show the results of $S = 3$ IS-PhCWGs. For lower frequencies such as $a/\lambda = 0.269$, there are bright CPs near the connection interface. However, due to the small group velocity and F-P resonance, the bend-transmittances are very low. At higher frequencies, the bright CPs inside the air holes disappear, thus no stable, bright CPs near the connection interface. The right six images in Fig.14 show the results of $S = 3$ IA-PhCWGs. For the $S = 3$ IA-PhCWGs, we find that at higher frequencies such as $a/\lambda = 0.272$ and $a/\lambda = 0.276$ there exist "stable", bright CPs near the connection interface. Interestingly, the bend-transmittances near these frequencies are relatively higher. We have observed that the $S = 3$ IA-PhCWG has higher bend-transmittance than the $S = 3$ IS-PhCWG overall. Maybe this is related to the "stable", bright CPs we have found in the $S = 3$ IA-PhCWGs. In addition, this is another case where the shapes of air holes mildly modify the location of CPs and affect the bend-transmittance when the domain-wall type is not changed.

To conclude our preliminary investigation into the circular polarization singularities, we have observed the existence of air-hole bright CPs in several high bend-transmittance bands and their disappearance in some low bend-transmittance bands. However, in $S = 2$ and $S = 3$ PhCWGs, there are bright CPs in the silicon region near the connection interface. We speculate that multiple CPs can appear inside the dielectric region with strong field intensity when the waveguide width is large. However, because they are exposed to a large area of uniform dielectric, these dielectric CPs can be unstable at the bends where the

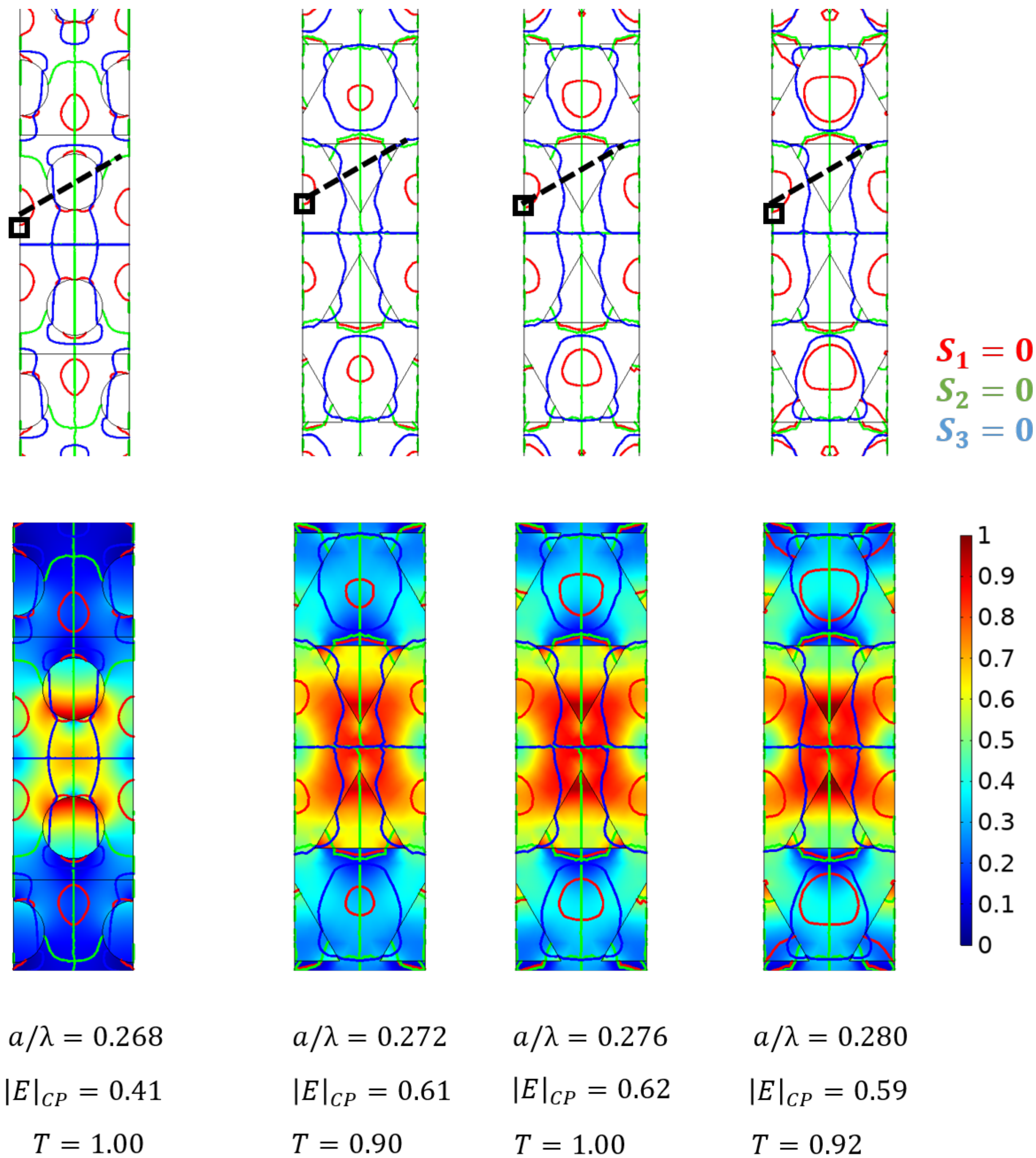

Figure 12. The zero-value isoline of Stokes parameters (top) and the Electric field amplitudes (bottom) of $S = 1$ IS-(left one column) and IA-(right three columns) PhCWGs. The corresponding frequencies, normalized E-field amplitudes at the location of CPs, and the bend-transmittance are shown below each plot.

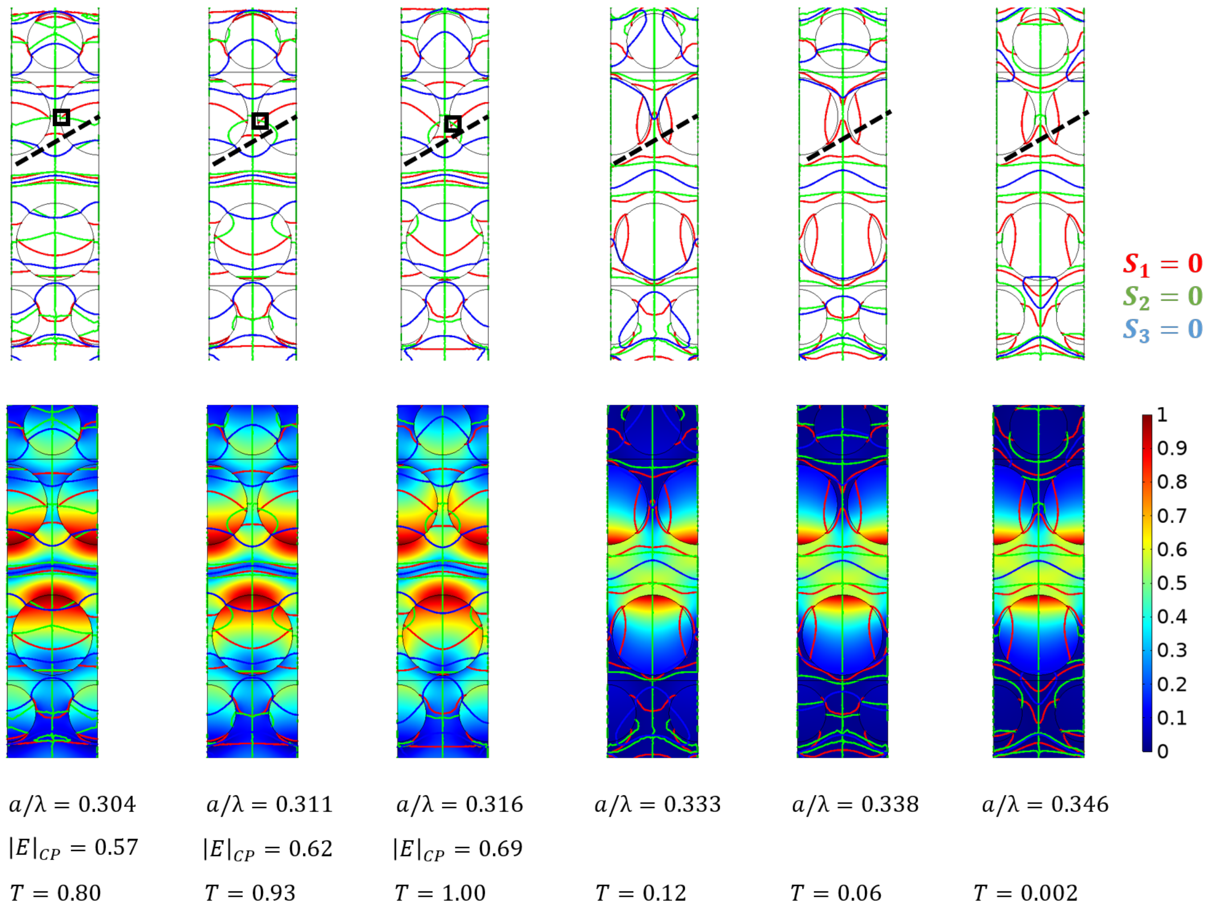

Figure 13. The zero-value isoline of Stokes parameters (top) and the Electric field amplitudes (bottom) of $S = 2$ IS-PhCWGs. The corresponding frequencies, normalized E-field amplitudes at the location of CPs, and the bend-transmittance are shown below each plot.

translational symmetry is broken. Furthermore, because the lattice configuration is more compact at the bends in narrower PhCWGs, CPs are less affected by the broken translational symmetry. The most important point is that CPs located inside the air holes disappear around the position where the bend-transmission abruptly decreases. This suggests that there is some correlation between the high bend-transmission and the existence of CPs.

Finally, we give an example that the bright CPs continue to exist inside the bending corners of a Z-shaped waveguide (Fig.15). In the high bend-transmittance band of $S = -2$ IA-PhCWG, we have confirmed the existence of bright CPs near the connection interface in the unit cell calculation. Here we investigate whether the same CPs persist in the bends if we excite the same waveguide mode in a Z-shaped waveguide. Like in the unit cell calculations, we identify the locations of CPs using the Stokes parameter isolines. The bright CPs near the bending corners are marked with black boxes. In the straight waveguide segment, we can find the bright CPs at the same location as those in the unit cell calculation. In the bends, we can see that there are strong distortions in the Stokes parameter isolines but the CPs (crossing nodes of red and green lines) exist in most of the air holes. After the light wave propagates through the second bend, the Stoke parameter isolines restore their shapes and the CPs are at the same location as before. While it is possible that the perturbation at the bends may give rise to accidental CPs. We believe this result demonstrates an uninterrupted distribution of the same type of CPs as we have identified in the unit cell calculation.

References

1. Ma, J., Xi, X. & Sun, X. Topological photonic integrated circuits based on valley kink states. *Laser & Photonics Rev.* **13**, 1900087, DOI: https://doi.org/10.1002/lpor.201900087 (2019). https://onlinelibrary.wiley.com/doi/pdf/10.1002/lpor.201900087.

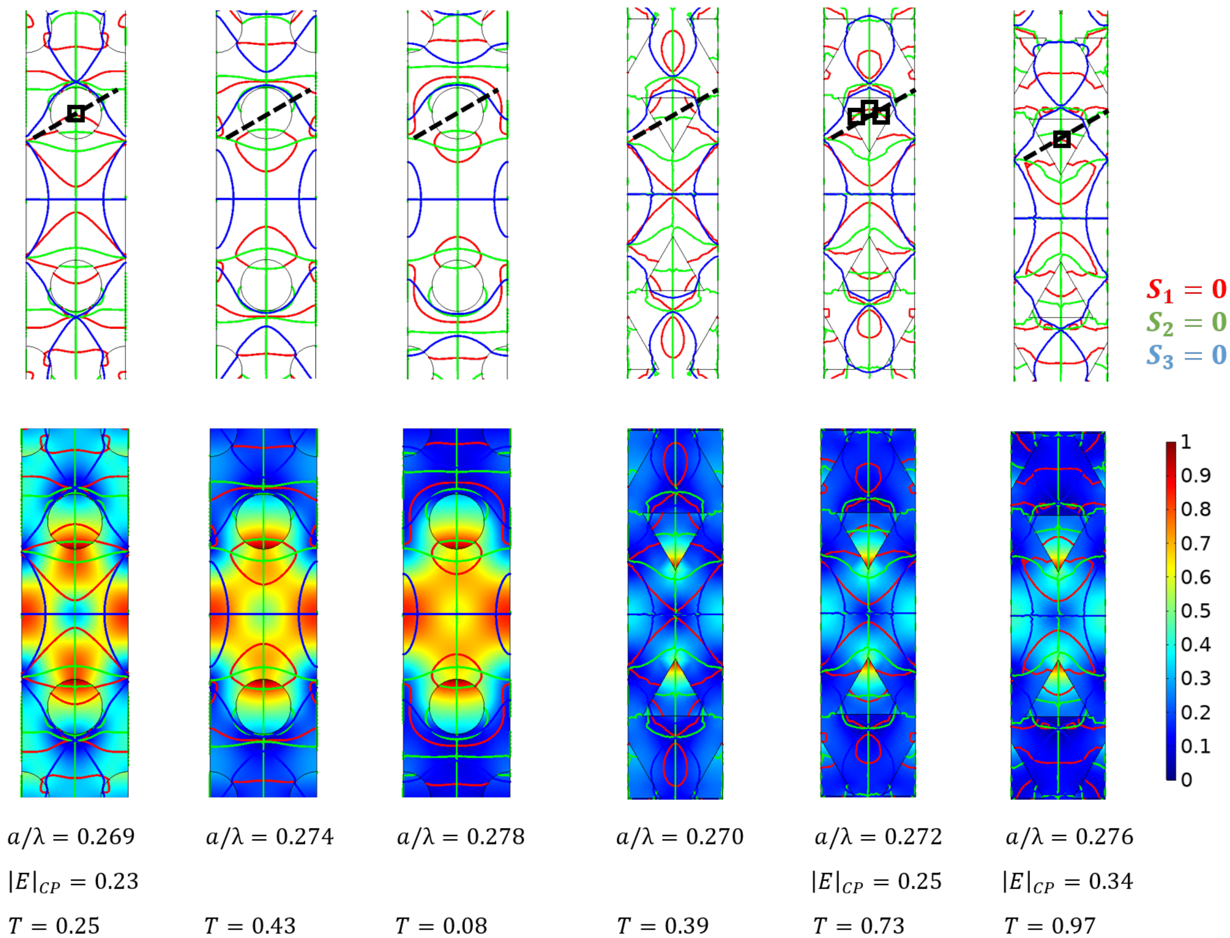

Figure 14. The zero-value isoline of Stokes parameters (top) and the Electric field amplitudes (bottom) of $S = 3$ IS-(left three columns) and IA-(right three columns) PhCWGs. The corresponding frequencies, normalized E-field amplitudes at the location of CPs, and the bend-transmittance are shown below each plot.

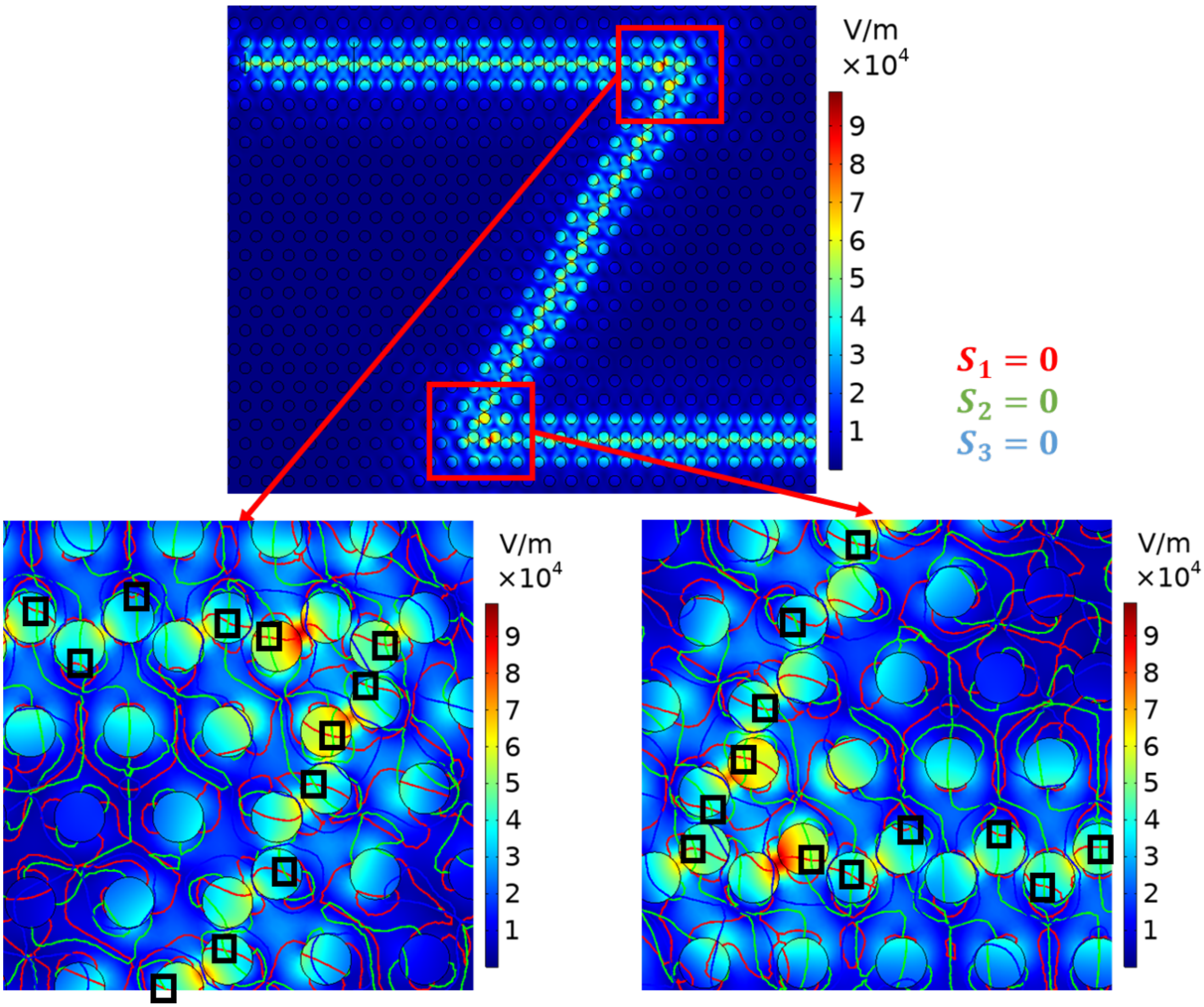

Figure 15. The electric filed amplitude and CP distribution of a Z-shaped $S = -2$ IS-PhCWG at frequency $a/\lambda = 0.291$. The locations of CPs are marked with black boxes.

2. Yamaguchi, T. *et al.* Gaas valley photonic crystal waveguide with light-emitting inas quantum dots. *Appl. Phys. Express* **12**, 062005, DOI: 10.7567/1882-0786/ab1cc5 (2019).

3. Shalaev, M. I., Walasik, W., Tsukernik, A., Xu, Y. & Litchinitser, N. M. Robust topologically protected transport in photonic crystals at telecommunication wavelengths. *Nat. nanotechnology* **14**, 31—34, DOI: 10.1038/s41565-018-0297-6 (2019).

4. Chen, X.-D., Zhao, F.-L., Chen, M. & Dong, J.-W. Valley-contrasting physics in all-dielectric photonic crystals: Orbital angular momentum and topological propagation. *Phys. Rev. B* **96**, 020202, DOI: 10.1103/PhysRevB.96.020202 (2017).

5. Kumar, A. *et al.* Phototunable chip-scale topological photonics: 160 gbps waveguide and demultiplexer for thz 6g communication. *Nat. Commun.* **13**, 5404, DOI: 10.1038/s41467-022-32909-6 (2022).

6. Arora, S., Bauer, T., Barczyk, R., Verhagen, E. & Kuipers, L. Direct quantification of topological protection in symmetry-protected photonic edge states at telecom wavelengths. *Light. Sci. & Appl.* **10**, 9, DOI: 10.1038/s41377-020-00458-6 (2021).

7. Yang, Y. *et al.* Terahertz topological photonics for on-chip communication. *Nat. Photonics* **14**, 446–451, DOI: 10.1038/s41566-020-0618-9 (2020).

8. He, X.-T. *et al.* Topological polarization beam splitter in dual-polarization all-dielectric valley photonic crystals. *Phys. Rev. Appl.* **18**, 044080, DOI: 10.1103/PhysRevApplied.18.044080 (2022).

9. Yoshimi, H., Yamaguchi, T., Ota, Y., Arakawa, Y. & Iwamoto, S. Slow light waveguides in topological valley photonic crystals. *Opt. Lett.* **45**, 2648–2651, DOI: 10.1364/OL.391764 (2020).

10. Gao, Z. *et al.* Valley surface-wave photonic crystal and its bulk/edge transport. *Phys. Rev. B* **96**, 201402, DOI: 10.1103/PhysRevB.96.201402 (2017).

11. Yoshimi, H. *et al.* Experimental demonstration of topological slow light waveguides in valley photonic crystals. *Opt. Express* **29**, 13441–13450, DOI: 10.1364/OE.422962 (2021).

12. Arregui, G., Gomis-Bresco, J., Sotomayor-Torres, C. M. & Garcia, P. D. Quantifying the robustness of topological slow light. *Phys. Rev. Lett.* **126**, 027403, DOI: 10.1103/PhysRevLett.126.027403 (2021).

13. Mehrabad, M. J. *et al.* Chiral topological photonics with an embedded quantum emitter. *Optica* **7**, 1690–1696, DOI: 10.1364/OPTICA.393035 (2020).